J. Fluid Mech. (2006), *vol.* 566, *pp.* 421–445.
doi:10.1017/S0022112006002102 Printed in the United Kingdom

The combination of electrospray and flow focusing

By ALFONSO M. GAÑÁN-CALVO, JOSÉ M. LÓPEZ-HERRERA AND PASCUAL RIESCO-CHUECA

E.S.I., Universidad de Sevilla, Camino de los Descubrimientos s/n, 41092 Spain

(Received 10 November 2003 and in revised form 11 April 2006)

An ultra-fine liquid atomization procedure combining the advantages of electrospray and flow focusing is presented. Both techniques are known to produce strikingly small and steady liquid micro-jets issuing from menisci held by capillary forces. Such menisci take the form of a cusp-like drop attached to the feeding tube (flow focusing: FF) or a Taylor cone (electrospray: ES). The issuing micro-jets are forced or 'sucked' from the parent meniscus either by pressure or electrohydrodynamic forces. Subsequent capillary breakup of the jet leads to fine sprays of remarkable quality. Here we describe the joint effect of pressurization and electrification in a flow focusing device, and the subsequent coupling of both ES and FF phenomena. For any given liquid and flow rate, the combined procedure gives rise to significantly smaller droplet sizes than observed in any of the source techniques. The co-flowing gas stream removes space charges; in addition, the perforated plate facing the feed tube provides an electric barrier, shielding the jet-meniscus or 'production' area from the spray or 'product' area. As a result, space charges and electrified droplets are removed from the production area, thus avoiding the ambient electric saturation which becomes a limiting factor in ES-spraying: a significantly enhanced spraying stability ensues, with a much wider operation range than FF or ES. Other unexpected outcomes from the combination are also shown. A theoretical model is developed to predict the emitted droplet size: a first integral of the momentum equation yielding a generalized Bernoulli equation, and an explicit approximation for the jet diameter and droplet size, accurate within a broad parametrical band.

1. Introduction

The fine dispersion of a liquid into a gas is necessary in most technologies involving chemical/biochemical processes and energy conversion. Our daily lives involve the (rather inefficient) atomization of a vast amount of liquid: ground transportation alone requires the atomization of an estimated global flow rate ranging from 100 to 300 $m^3\,s^{-1}$ on earth. Most processes requiring liquid atomization would be significantly optimized were the droplet size spectrum tailored at will.

Micron and sub-micron monodisperse spray production is currently the object of intensive research. Scientific and technological applications range from material science (Berkland, Pack & Kim 2004), energy (combustion) (Jayan & Raghunandan 2003), analytical chemistry (Fenn *et al.* 1989), industrial chemistry (Lawley & Leatham 1999), pharmacology (Howard & Alpar 2002), medicine and biomedicine (Gautam, Waldrep & Densmore 2003) to agriculture (dispersion of insecticides and

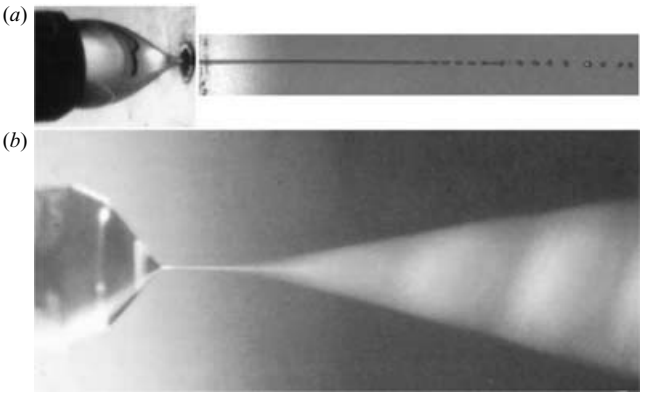

FIGURE 1. (*a*) Photograph of a flow focusing device, showing the feed tube (left), the cusp-like liquid meniscus focused by the gas stream, and the issuing liquid micro-jet (right) (Gañán-Calvo 1998, adapted). (*b*) A typical cone–jet electrospray configuration: feeding tip, conical liquid meniscus and issuing spray (Pantano, Gañán-Calvo & Barrero 1994).

phytosanitary products (Laryea & No 2003). A comprehensive overview of droplet applications, mainly in the field of analytical chemistry, is provided by Basaran (2002). Specific journals and books are devoted to aerosol production (Lefevbre 1989; Bailey 1988). Some shortcomings of current atomization methods could be overcome by introducing a technique allowing ultra-fine, controllable, robust and scalable aerosol production. Such potential can be expected from the present electro-flow-focusing (EFF) technique, opening the door to widespread application in micro-engines, micro-reactors, thin films, biomedicine, chemical and biochemical analysis and other fields.

Optimal liquid atomization requires a continuous energy supply triggering liquid bulk disruption into the desired droplet spectrum. Current methods leading to controllable micron and sub-micron mono-disperse droplets are few. Basaran (2002) examines the main available options: electrospray (ES), selective withdrawal (Cohen *et al.* 2001) and flow focusing (FF) (Gañán-Calvo 1998); all of these exhibit to some degree, simplicity, reproducibility and physical universality, and are therefore suitable for a variety of applications, among them the production of emulsions and micro- or nano-encapsulation. Given a target droplet size, FF is in addition characterized by its robustness, insensitivity to the electrical properties of the liquid, simple scalability and relatively large spray yield.

Although drawing on different energy sources, FF and ES share a similar physics governing the micro-jet formation, stability and breakup. The jets produced by both methods are issued by mechanical or electrostatic local 'suction' operating under specific geometrical constrictions. In FF, a strongly convergent gas flow through a small orifice defines the local conditions (strong pressure gradient at the exit orifice) sustaining the emission of a steady micro-jet. A jet is issued through the orifice when the liquid is fed in the vicinity of the orifice by a variety of means (capillary tube, channel, porous tip and so on; see figure 1*a*). In ES, a pre-condition for the 'suction' effects is the occurrence of a universal configuration: a conical liquid meniscus, held by electrostatic forces (Taylor 1964). Provided the liquid properties are adequate, the tip of the liquid cone is urged by forces strong enough to bring out a continuous liquid emission in the form of a steady micro-jet eventually breaking up into a fine spray (see figure 1*b*).

When both methods are analysed (Cloupeau & Prunet-Foch 1989; Fernández de la Mora & Loscertales 1994; Rosell-Llompart & Fernández de la Mora 1994; Gañán-Calvo, Dávila & Barrero 1997; Gañán-Calvo 1998, 1999; Cherney 1999*a*, *b*; Gañán-Calvo & Barrero 1999, among others), it is ostensible that the particularly desirable spray features induced by ES and FF are linked to the breakup pattern. Upon breakup, the droplet size depends on the microjet diameter and the ratio of the external driving forces to the surface tension forces (López-Herrera, Gañán-Calvo & Pérez-Saborid 1999; Gordillo, Pérez-Saborid & Gañán-Calvo 2001).

Furthermore, once the micro-jet issues, it is still under the influence of the same forces that are responsible for its production. In FF, the surrounding gas stream, flowing axially beyond the orifice exit, causes a strong shear force on the jet. In ES jets, the surface charge at the liquid–gas interface is subsequently pulled by the external electrostatic field. Depending of the relative intensity of these forces compared to the surface tension force (see Eggers (1997) for a very complete overview on the physics of the jet breakup), the microjet may show (i) a Rayleigh type, capillary axisymmetric breakup yielding remarkably good spray size monodispersity provided the capillary forces are large enough, or (ii) a hydrodynamic instability with a subsequent non-symmetric breakup, leading to a more or less intense cascade of further droplet disruptions, yielding a poorer size dispersion, but smaller droplet size as in a pure capillary breakup (Cloupeau & Prunet-Foch 1994; Rosell-Llompart & Fernández de la Mora 1994; Chen, Pui & Kaufman 1995; Gordillo *et al.* 2001).

After both ES and FF have been investigated and sufficiently understood in terms of their relevant geometrical features (Fernández de la Mora & Loscertales 1994; Gañán-Calvo *et al.* 1994; Gañán-Calvo 1998), a judicious initiative is the study of their combination. In particular, it is important to understand how the two energy sources (electrical and mechanical) combine in a physically consistent way to yield a substantial reduction in droplet size. The aim of the present work is therefore to arrive at some guidelines and initial conclusions about the said combination. A welcome result from the analysis is a first integral of the momentum equation in the axial direction, providing a closed expression for the resulting spray droplet size.

2. The electro-flow focusing (EFF) configuration and parameters

When an electric voltage drop is applied between the liquid and the focusing orifice in a genuine FF configuration (see figure 2), free charges in the liquid bulk are induced and move under the action of the resulting electric field. It has been well established (Landau & Lifshitz 1960; Melcher 1981; Saville 1997) that free charges migrate to the liquid–gas interface and form a quasi-equilibrium layer whenever the electric relaxation time ε_i/K is sufficiently shorter than any other characteristic hydrodynamic time, ε_i and K being the electrical permittivity and conductivity of the liquid. We focus here on the cases where this condition is met; indeed, the same condition must hold for electrospray to be feasible (Gañán-Calvo *et al.* 1994, 1997; Gañán-Calvo 1997*a*, *b*, 1999). As will be shown, obvious advantages result from this approach: the guaranteed existence of steady configurations (evidenced by experiments, see figure 3) and a simpler problem formulation.

We will study the spray size and the issued electric current. In the following, we present an experimental study under the guidance of a formal theoretical analysis of the problem.

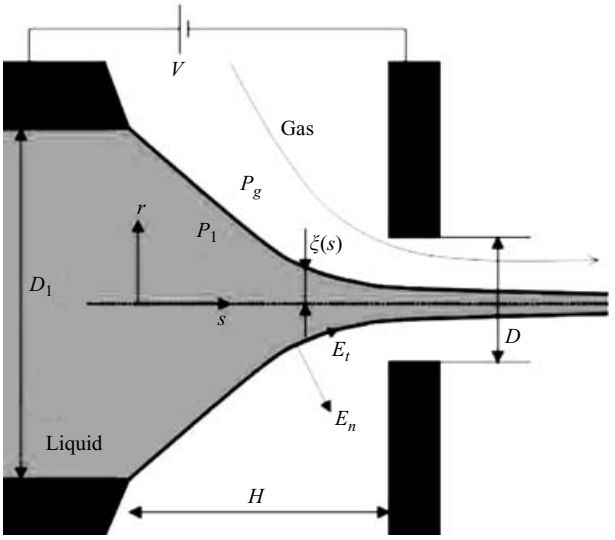

FIGURE 2. The electro-flow focusing (EFF) configuration under study.

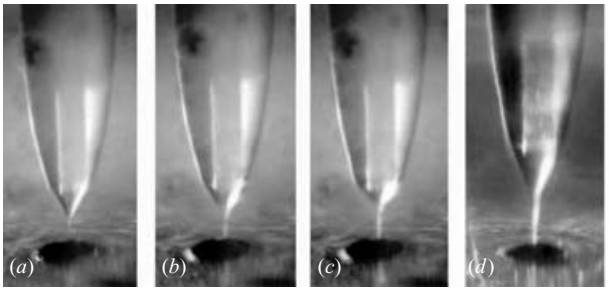

FIGURE 3. Some EFF examples. Liquid: water (electrical conductivity $K = 0.27\,\mathrm{S\,m^{-1}}$) $D = D_1 = 200\,\mu\mathrm{m}$; (*a*) $H = 250\,\mu\mathrm{m}$, $Q = 0.08\,\mu\mathrm{s}^{-1}$, $\Delta P = 257\,\mathrm{mbar}$, $V = 2200\,\mathrm{V}$; (*b*) $H = 250\,\mu\mathrm{m}$, $Q = 0.2\,\mu\mathrm{l\,s^{-1}}$, $\Delta P = 257\,\mathrm{mbar}$, $V = 2650\,\mathrm{V}$; (*c*) $H = 250\,\mu\mathrm{m}$, $Q = 0.4\,\mu\mathrm{l\,s^{-1}}$, $\Delta P = 257\,\mathrm{mbar}$, $V = 3400\,\mathrm{V}$; (*d*) $H = 380\,\mu\mathrm{m}$, $Q = 0.47\,\mu\mathrm{l\,s^{-1}}$, $\Delta P = 883\,\mathrm{mbar}$, $V = 2700\,\mathrm{V}$. Pictures taken with device S200G.

2.1. *Experimental methods*

Three different FF devices have been used (see figure 4). We assessed the influence of the exit orifice diameter D, the distance H from the feeding capillary tip to the orifice, and the capillary tip diameter D_1 on the issuing droplet size and charge. The number N of orifices per device has also been considered: $N = 1$ in devices S50 and S200G, and $N = 55$ in device D55. This parameter, however, requires a further in-depth analysis exceeding the scope of the present work. The feed tube is a silica capillary from Polymicro (OD 365 μm) with ID 75 μm and total length $L = 35\,\mathrm{mm}$ in the S50 and S200G devices, and with ID 40 μm and total length $L = 5\,\mathrm{mm}$ in the D55 device. We choose silica as a material for the feed tube to avoid potential gas ionization and corona discharges at the uneven micro-scale (border irregularities) of the tip.

On the other hand, we also studied the influence of some key liquid properties: density ρ, viscosity μ, surface tension σ and electrical conductivity K (see table 1).

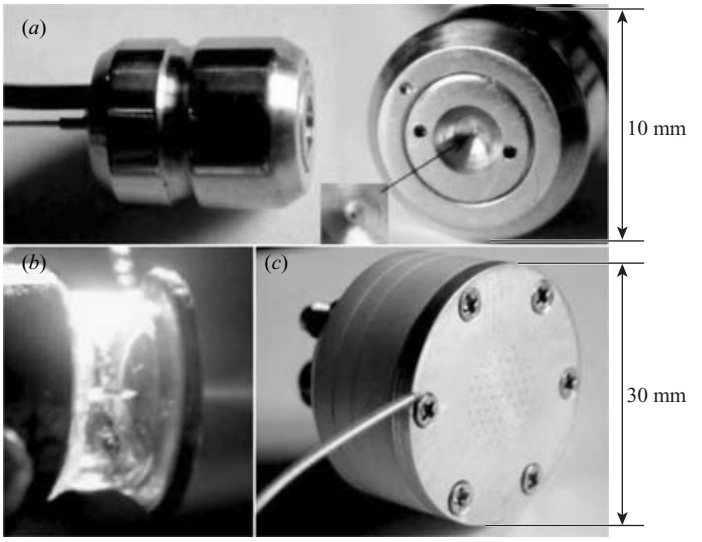

FIGURE 4. The three devices used in this study. (*a*) S50 device: a single ($N = 1$) orifice with $D = 50\,\mu\text{m}$, $D_1 = 120\,\mu\text{m}$, selectable H. (*b*) S200G device: the same configuration as S50, plus a glass window to inspect interior flow; $D = 200\,\mu\text{m}$. (*c*) D55 device: $N = 55$ orifices, $D = 200\,\mu\text{m}$, $D_1 = 365\,\mu\text{m}$. The distance H is selectable.

Liquid	σ (N m^{-1})	ρ (kg m^{-1})	K (S m^{-1})	μ (Pa s)
Water	0.072	1000	1.5×10^{-3}	0.0011
Ethanol	0.022	805	1.1×10^{-4}	0.0013
W/E 70/30 % vv	0.039	938	1.4×10^{-3}	0.002
W/E 30/70 % vv	0.0262	858	5.0×10^{-4}	0.00224
W/E 10/90 % vv	0.0476	824	4.3×10^{-4}	0.00178

TABLE 1. Liquid properties as measured at 23 °C. W/E are water/ethanol mixtures.

Surface tension was measured with a Krüss digital tensiometer using the Wilhelmy plate method; viscosity, with a digital Brookfield viscometer. Liquid electrical conductivity was determined by measuring the resistance of liquid-filled Tygon tubes (Cole & Parmer Tygon tubing OD 2 mm, ID 0.25 mm, variable length). We will not pay much attention to the liquid permittivity $\varepsilon_i = \beta\varepsilon_o$ (ε_o is the permittivity of vacuum) since it has been established that its influence on the droplet size and charge is generally negligible provided stable cone–jet ES conditions are met (Gañán-Calvo 1997*a*, 1999). We will not address such exceptional cases as the spraying of a very small flow rate of large permittivity liquids (β above 50) (Higuera 2003). This exceptional situation is described as the IP-regime in Gañán-Calvo (1999, 2004), with $Q < (\sigma\varepsilon_i)/(\rho K)$, a condition implying extremely small liquid flow rate since high electrical permittivity liquids exhibit a high electrical conductivity as well, owing to their polarity and their ability to dissolve ionic dissociable species.

Finally, the influence of the three essential input parameters of the system, the liquid flow rate Q, the applied gas pressure drop through the orifice Δp_g, and the applied liquid-to-orifice voltage drop V, is analysed in detail.

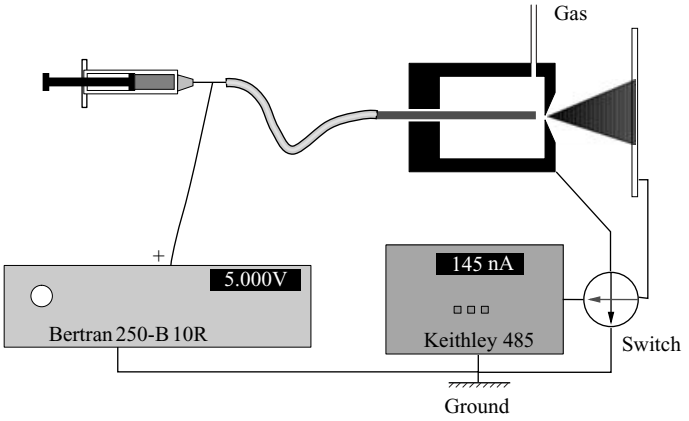

FIGURE 5. Typical electrical set-up used. The high-voltage power supply is at the left-hand bottom corner, and the pico-ammeter is shown at the right-hand bottom corner.

The liquids were infused with a syringe pump Harvard Apparatus Model 44 and different syringes (Harvard Apparatus 8 cc stainless steel syringe, Hamilton Gastight and Becton Dickinson plastic) depending on the required liquid flow rate. The focusing gas was always chosen to be air, supplied by a conventional laboratory pressurization system (brand Air Liquid). The electrical high voltage is provided by a Bertan 250-B 10R power supply. Both positive and negative polarity have been used in the study.

An impaction plate collects the electric current carried by the main droplets which is measured with a pico-ammeter (model 485 from Keithley). The plate is large enough to guarantee droplet impaction and collection. Full collection is checked by plotting the current deposited by the droplets against the distance from the issuing orifice of the nebulizer to the impaction plate. As the distance decreases, an asymptote or plateau is reached (in most cases, 10 to 15 mm is sufficient), thereby ensuring that full spray impaction is approximately achieved. In addition, we determine the occurrence of electrical discharges through the gas between the issuing liquid jet and the orifice edge by measuring the electric current collected at the orifice plate. There is a switch to select which electric current is measured (either from the impaction plate or from the orifice plate). Thus, the total electric current fed by the power supply is the sum of both electric currents. The electrical resistance of the liquid column inside the silica tubing must be calculated, because the total voltage V_T is applied to the liquid upstream of the feed tube (see figure 5). In order to evaluate the effective liquid voltage at the silica tip, V (see figures 2, 3 and 5), the total electric current passing through the liquid line is multiplied by the resistance, and subtracted from the total applied voltage V_T.

Droplets were monitored with a laser diffraction Sympatec Helos/BF Magic droplet sizing instrument, with R2 optics (from 0.5 to 85 μm) and Mie correction. Droplet size and charge are measured at the same time, following this routine: the impaction plate is separated from the nebulizer, and the spray is directed to the laser beam. Size measurements are taken at a distance from the orifice exit where no significant variation in the axial direction is observed, i.e. where the droplet size probability distribution function can be assumed to be relaxed (Lasheras, Villermaux & Hopfinger 1998).

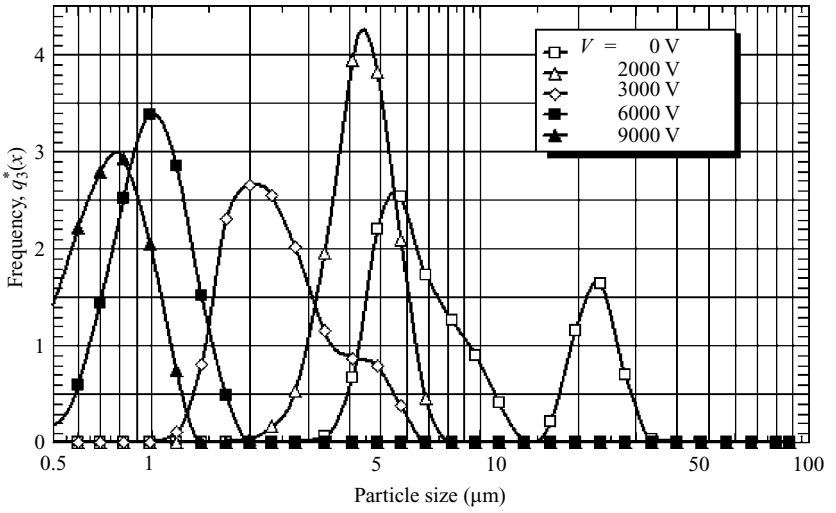

FIGURE 6. Droplet size distribution as a function of the applied voltage for ethanol, $Q = 75\,\mu l\,h^{-1}$, $\Delta p_g = 636\,mbar$, device S50 ($D = 50\,\mu m$, $H = 40\,\mu m$).

2.2. *Experimental results. Droplet size and charge measurements*

First, we measured the droplet size distribution, determining the mass median diameter d_{50} (in μm), and the geometric standard deviation GSD as a function of the three main parameters of the problem (liquid flow rate Q, gas pressure drop Δp_g, and total applied voltage V_T). To represent the size distribution we followed the ISO 9276 recommendation, plotting the dimensionless quantity $q_3^*(x)$ as a function of the particle size x. $q_3^*(x)$ is a logarithmic density representation from a discrete Sympatec measurement set:

$$q_3^*(x_i) = \frac{\Delta Q_{3,i}}{\ln x_i - \ln x_{i-1}}, \tag{2.1}$$

where $\Delta Q_{3,i}$ is the fraction of the total volume associated with droplets whose radius lies between x_i and x_{i-1}. About two thousand measurements have been carried out.

As a first remark, consistent, sub-micron size sprays can be produced with our devices. In particular, we measured size decreases owing to electrification down to a mere 7 % of the zero-voltage (FF) size.

Figures 6 and 7 show the effect of electrification on the droplet size distribution, under two widely opposed flow-rate situations (small and large Q). Figure 6 shows the droplet size distribution for a given liquid flow rate ($Q = 75\,\mu l\,h^{-1}$) and pressure drop ($\Delta p_g = 636\,mbar$), using ethanol and device S50 ($D = 50\,\mu m$, $H = 40\,\mu m$), under different voltages. It can be observed in figure 7 that under large flow-rate, electrification is unable to produce significant droplet size reduction. Indeed, an electric field is unable to modify the electric loads at the jet surface whenever the aerodynamic or residence time $t_R \sim H/v_o$ is small compared with the electrical relaxation time $t_e \sim \varepsilon_i/K$, where $\varepsilon_i = \beta\varepsilon_o$ and K are the electrical permittivity and conductivity of the liquid. As a general rule, the larger the flow rate, the more ineffective the electrification is in terms of droplet size reduction.

On the other hand, figure 6 provides an instance of successful electrification, under moderate flow rate. The unelectrified curve is unstable: note the bimodal distribution, hinting at a dripping phenomenon, associated with a low Weber number (the double-peak distribution is caused by pulsation). As an electric field is applied, the effect is

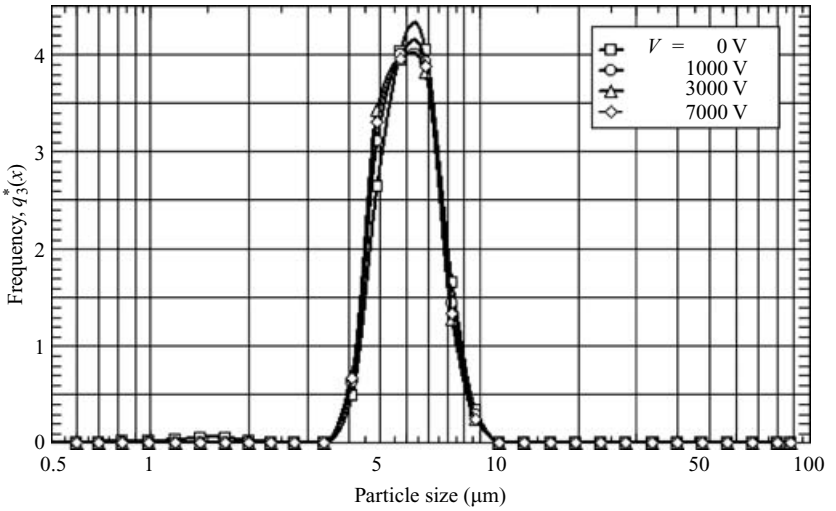

FIGURE 7. Droplet size distribution as a function of the applied voltage for ethanol, $Q = 750\,\mu l\,h^{-1}$, $\Delta p_g = 640$ mbar, device S50 ($D = 50\,\mu m$, $H = 40\,\mu m$).

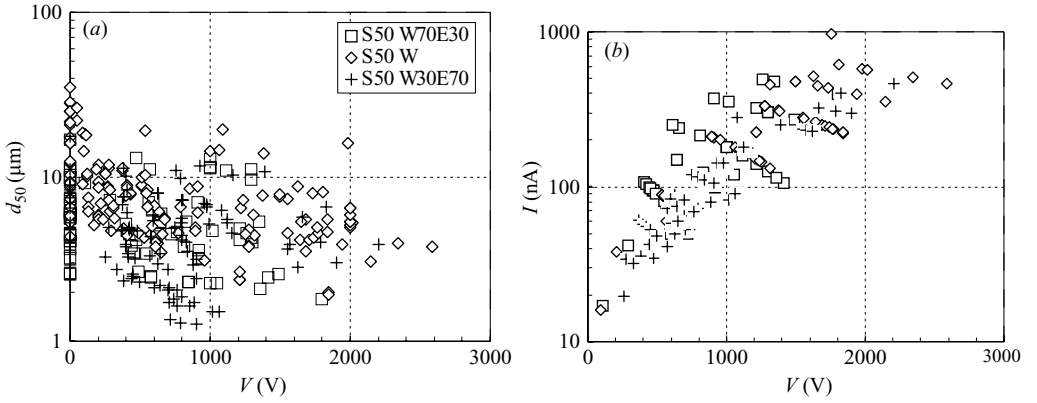

FIGURE 8. (*a*) Droplet size d_{50} and (*b*) total electric current I as a function of the effective voltage V for several values of the gas pressure drop Δp (from 0 to 4 bar) and flow rate Q (W70E30: from 0.3 to $3\,ml\,h^{-1}$; W30E70: from 0.2 to $3\,ml\,h^{-1}$; water: from 0.3 to $5\,ml\,h^{-1}$).

an increase of the effective Weber number owing to the coupled effect of the applied gas pressure and the electric field, causing a transition into the jetting, axisymmetric breakup regime (conspicuously single-peaked distribution: see 2000 V curve, open triangle symbol). Further increases in the applied voltage lead to smaller droplets.

This example illustrates the substantial droplet size reduction (above one order of magnitude) to be obtained by combining FF and ES. In general, we have observed a significant droplet size reduction with the applied voltage when the flow rate is kept small.

Figure 8 plots the droplet size d_{50} and total electric current I in device S50 as a function of the effective voltage V using three different liquids and several values of the gas pressure drop Δp and flow rate Q. A single letter E or W refers to pure ethanol or pure water, respectively, while mixtures are labelled with a percentage code

(e.g. 'W30E70' indicates water/ethanol 30/70 % vv). Figure 8 shows a general trend: as the voltage increases, the droplet size decreases and the current transported by the jet increases. However, the large number of free parameters related to the proposed procedure makes it difficult to extricate from the raw data the physics of the process. All the raw data will be analysed in detail below with the help of a suitable electrohydrodynamic theoretical model predicting the emitted droplet size.

3. Theoretical analysis

An analytical approach involves solving the steady Navier–Stokes equations for the liquid, and the Euler equations for the gas stream, assuming it incompressible:

$$\begin{aligned} &\nabla\cdot\boldsymbol{v}=0, \quad \rho\boldsymbol{v}\cdot\nabla\boldsymbol{v}=-\nabla p+\nabla\cdot\tau', \\ &\nabla\cdot\boldsymbol{v}_g=0, \quad \rho_g\frac{(\boldsymbol{v}_g\cdot\boldsymbol{v}_g)^2}{2}+p_g=p_{go}, \end{aligned} \tag{3.1}$$

where $\boldsymbol{v}$ and $\boldsymbol{v}_g$ are the liquid and the gas velocity; p, p_g and p_{go} are the liquid and gas pressure and the gas stagnant pressure; and $\tau'=\mu[\nabla\boldsymbol{v}+(\nabla\boldsymbol{v})^T]$ is the liquid viscous stress tensor. The bulk equations for the liquid and the gas are coupled through the interfacial boundary conditions, namely the balance of the normal and tangential stresses at the surface $r=\xi(s)$,

$$\left.\begin{aligned} &p-p_g-\boldsymbol{e}_n\cdot\tau\cdot\boldsymbol{e}_n+\boldsymbol{e}_n\cdot\left(\tau_e^o-\tau_e^i\right)\cdot\boldsymbol{e}_n=\sigma\nabla\cdot\boldsymbol{e}_n, \\ &\boldsymbol{e}_n\cdot\tau\cdot\boldsymbol{e}_t-\boldsymbol{e}_n\cdot\left(\tau_e^o-\tau_e^i\right)\cdot\boldsymbol{e}_t=0, \\ &\tau_e^j=\varepsilon_j\left(\boldsymbol{E}^j\boldsymbol{E}^j-\frac{|\boldsymbol{E}^j|^2}{2}\boldsymbol{I}\right), \end{aligned}\right\} \tag{3.2}$$

where τ_e^j, $\boldsymbol{E}^j$ and ε_j are the Maxwell electric stress tensor, electric field and permittivity for the j phase (the $j=o,i$ superindex denotes the gas phase and the liquid phase); $\boldsymbol{I}$ is the unity tensor, σ the surface tension, $\boldsymbol{e}_n$ and $\boldsymbol{e}_t$ are the unit vectors normal and tangential to the interface. In the above boundary conditions (3.2), the gas viscous forces were neglected.

The complexity of the physical ingredients in play lead to the present model, where the electric part is drastically simplified, and the upstream and downstream boundary conditions are not expressed. A large number of dimensionless groups are involved here, as can be judged by the discussion in Gañán-Calvo (1998, 2004) and López-Herrera, Riesco-Chueca & Gañán-Calvo (2005). The above may give an idea of the computational difficulties inherent to a comprehensive three-dimensional model. A diversity of approaches is found in works dealing with similar free-surface problems such as the formation of drops and jets from a nozzle under several conditions: unelectrified, inviscid liquid (Schulkes 1994); unelectrified, highly viscous (Zhang & Stone 1997); unelectrified, moderately viscous (Wilkes, Phillips & Basaran 1999); axially electrified, inviscid and conducting liquid (Notz & Basaran 1999).

To circumvent computational pitfalls it is a common practice to approximate the liquid dynamics by one-dimensional models, taking advantage of the slenderness of the phenomena. The one-dimensional approximation has proved extremely successful in free-surface problems (Lee 1974; Eggers & Dupont 1994; García & Castellanos 1994; López-Herrera *et al.* 1999; Yildirim & Basaran 2001; López-Herrera & Gañán-Calvo 2004) and can be derived formally by Taylor-expansion in the radial direction r (s is the axial direction) the radial and axial velocity $u(r,s)$, $w(r,s)$ and the pressure $p(r,s)$

of the liquid:

$$\left.\begin{aligned} w(r,s) &= w_o(s) + \tfrac{1}{2}r^2 w_2(s) + \cdots, \\ u(r,s) &= -\tfrac{1}{2}r\frac{\mathrm{d}w_o(s)}{\mathrm{d}s} - \tfrac{1}{8}r^3\frac{\mathrm{d}w_2(s)}{\mathrm{d}s}\cdots, \\ p(r,s) &= p_o(s) + \tfrac{1}{2}r^2 p_2(s) + \cdots. \end{aligned}\right\} \tag{3.3}$$

Upon insertion and lowest-order truncation in the bulk equations, ordinary differential equations are obtained; a detailed derivation can be found in Eggers & Dupont (1994) and García & Castellanos (1994) (uncharged jets) or in López-Herrera *et al.* (2005) (charged jets). Averaging the axial momentum balance of a jet slice leads to similar results (Melcher & Warren 1971; Gañán-Calvo *et al.* 1997; Feng 2002). The success of the approximation is ensured when viscous diffusion of momentum from the liquid surface is large enough to flatten the liquid axial velocity profile (Gañán-Calvo 1997*a*, 1999; Gordillo *et al.* 2001). López-Herrera *et al.* (2005) have explored the conditions ruling the occurrence of markedly inhomogeneous velocity profiles (including the possibility of a boundary layer at the interface). This happens when poor liquid conductors are accelerated into a jet. Such liquids would not be preferred for EFF applications.

As a summary, the one-dimensional slender approximation collapses the three-dimensional bulk momentum equations and the interfacial stress boundary conditions into a single equation, an axial momentum equation for the unknown average axial velocity $w_o(s)$,

$$\frac{\mathrm{d}}{\mathrm{d}s}\left(\frac{\rho w_o^2}{2} + p_g + \sigma\nabla\cdot\boldsymbol{n} - \boldsymbol{e}_n\cdot\left(\tau_e^o - \tau_e^i\right)\cdot\boldsymbol{e}_n\right) = \frac{3\mu}{\xi^2}\frac{\mathrm{d}(\xi^2\dot{w}_o)}{\mathrm{d}s} + \frac{2\pi\xi\left(\boldsymbol{e}_n\cdot\left(\tau_e^o - \tau_e^i\right)\cdot\boldsymbol{e}_t\right)}{\pi\xi^2(s)}, \tag{3.4}$$

where the dot stands for the axial derivative $\mathrm{d}/\mathrm{d}s$ and $\xi(s)$ is the local radius of the jet.

Similarly, the slenderness of our jet configuration (see figure 2) opens the door to one-dimensional conservation equations of mass ($Q = \pi\xi^2 w_o$), momentum and charge. Additionally, under the assumption that the electric relaxation time $t_e = \varepsilon_i/K$ is sufficiently smaller than any other characteristic time of the process, the normal electric field in the bulk of the liquid and at the interface can be assumed negligible $E_n^i \simeq 0$ (Gañán-Calvo *et al.* 1994, 1997; Gañán-Calvo 1997*a*, *b*, 1999). Therefore, $\boldsymbol{e}_n\cdot(\tau_e^o - \tau_e^i)\cdot\boldsymbol{e}_t = (\varepsilon_o E_n - \varepsilon_i E_n^i)E_s \simeq \varepsilon_o E_n E_s$, where E_n and E_s are the normal and the tangential electric fields at the jet surface. In addition, $\boldsymbol{e}_n\cdot(\tau_e^o - \tau_e^i)\cdot\boldsymbol{e}_n = [E_n^2 - \beta E_s^{i2} + (\beta-1)E_s^2]/2 \simeq [E_n^2 + (\beta-1)E_s^2]/2$.

Under these assumptions, a closed one-dimensional axial momentum balance is obtained:

$$\frac{\mathrm{d}}{\mathrm{d}s}\left(\frac{\sigma}{\xi} + \frac{1}{2\pi^2}\frac{\rho Q^2}{\xi^4}\right) + \frac{6\mu Q}{\pi\xi^2}\frac{\mathrm{d}}{\mathrm{d}s}\left(\frac{\dot{\xi}}{\xi}\right) = -\frac{\mathrm{d}p_g}{\mathrm{d}s} + \frac{2\varepsilon_o E_n E_s}{\xi} + \frac{\varepsilon_o}{2}\frac{\mathrm{d}}{\mathrm{d}s}\left[E_n^2 + (\beta-1)E_s^2\right]. \tag{3.5}$$

The three terms of the left-hand side can be interpreted as three *momentum sinks* of the system: (i) the axial resultant of the surface tension force, (ii) the liquid inertia, and (iii) the viscous resistance in the axial direction s. Correspondingly, the other three terms on the right-hand side are *momentum sources*: (i) the axial resultant of the externally applied gas pressure $p_g(s)$, (ii) the axial component of the tangential

electrostatic surface stress, and (iii) the axial resultant of the normal electrostatic surface stress (the electrostatic suction plus the polarization force).

In order to evaluate the electric field, the Laplace differential equation for the electric potential could be solved, $\nabla^2\Phi = 0$. Alternatively, Coulomb's law provides an integral equation where the electric potential is expressed in terms of an unknown line-charge distribution $A(s)$ at the axis,

$$\Phi(r, s) = \frac{1}{4\pi\varepsilon_o}\int_{-\infty}^{\infty}\frac{A(s')\,\mathrm{d}s'}{(s-s')^2 + r^2}. \tag{3.6}$$

Slenderness is assumed, $s \gg r \sim \xi(s)$; the above expression is particularized at the jet surface $r = \xi(s)$, and the line charge distribution $A(s)$ is written as a function of the normal electric field E_n, $A(s) = 2\pi\xi\,\sigma_e = 2\pi\varepsilon_o\,\xi E_n$, σ_e being the surface charge distribution. This yields:

$$\begin{aligned} E_s(s) = -\frac{\mathrm{d}\Phi(s)}{\mathrm{d}s} &= -\frac{\mathrm{d}}{\mathrm{d}s}\int_{-\infty}^{\infty}\frac{\xi(s')E_n(s')\,\mathrm{d}s'}{2[(s-s')^2 + \xi^2(s)]^{1/2}} \\ &= \int_{-\infty}^{\infty}\frac{\left[(s-s') + \xi(s)\dot{\xi}(s)\right]\xi(s')E_n(s')\,\mathrm{d}s'}{2[(s-s')^2 + \xi^2(s)]^{3/2}}. \end{aligned} \tag{3.7}$$

This integral converges along the whole region of interest of this study; it can be shown (Hohman *et al.* 2001; Feng 2002) that it becomes negligibly small as the liquid jet thickens upstream to merge with the liquid meniscus at the tip of the feeding tube (figure 2), a result that should be sufficient for the scope of our analysis.

On the other hand, assuming that the surrounding gas conduction effects are negligible (this can be subsequently verified), the charge conservation can be written as:

$$I = \pi K E_s\xi^2 + 2Q\varepsilon_o E_n\xi^{-1}, \tag{3.8}$$

assuming that liquid surface velocity does not differ siquificantly from bulk velocity, where I is the total electric current driven by the liquid jet. From the analytical and computational point of view, equations (3.5) to (3.8) formally close the problem for the unknowns ξ, E_n and E_s, together with some appropriate boundary conditions upstream at the tip of the feeding tube and downstream at the plate orifice,

$$\xi(0) = D_1/2, \quad \dot{\xi}(H) = 0, \tag{3.9}$$

where D_1 is the feed tube diameter. The boundary condition at the plate expresses the absence of any 'thinning' force beyond the orifice.

The boundary conditions for the electric field are (i) the value of the normal electric field at $s = 0$, consistently calculated from the liquid potential V at the tip of the feeding tube, (ii) the given geometry, and (iii) $E_s = 0$ at the plate orifice ($s = H$).

Combining equations (3.5) and (3.8), a useful expression results:

$$\begin{aligned} \frac{\mathrm{d}}{\mathrm{d}s}\left[\frac{\sigma}{\xi} + \frac{1}{2\pi^2}\frac{\rho Q^2}{\xi^4} + P_g + \frac{I\Phi}{Q} - \frac{\varepsilon_o}{2}\left(E_n^2 + (\beta-1)E_s^2\right)\right] + \frac{6\mu Q}{\pi\xi^2}\frac{\mathrm{d}}{\mathrm{d}s}\left(\frac{\dot{\xi}}{\xi}\right) \\ = -\frac{\pi K}{Q}\left(\xi\frac{\mathrm{d}\Phi}{\mathrm{d}s}\right)^2, \end{aligned} \tag{3.10}$$

since $E_s = -\mathrm{d}\Phi/\mathrm{d}s$. A simplified version of this balance is used by Gamero-Castaño and Hruby (2002).

Let us give a physical interpretation for the right-hand side term of (3.10). The liquid jet can be thought of as a variable geometry resistor whose elemental resistance

is:

$$\mathrm{d}\Omega = \frac{\mathrm{d}s}{\pi K \xi^2}. \tag{3.11}$$

Thus, we can write:

$$\frac{\pi K}{Q}\left(\xi \frac{\mathrm{d}\Phi}{\mathrm{d}s}\right)^2 = \frac{1}{Q}\left(\frac{\mathrm{d}\Phi}{\mathrm{d}\Omega}\right)^2 \frac{\mathrm{d}\Omega}{\mathrm{d}s}, \tag{3.12}$$

$$\frac{\mathrm{d}\Phi}{\mathrm{d}\Omega} = -I_{cond}, \tag{3.13}$$

where $I_{cond} = \pi K \xi^2 E_s$ is the bulk electric conduction current. The Joule effect dissipates into heat an elemental electric power per element of resistor given by

$$\mathrm{d}W_J = I_{cond}^2 \, \mathrm{d}\Omega. \tag{3.14}$$

Therefore,

$$\frac{\mathrm{d}}{\mathrm{d}s}\left(\frac{\sigma}{\xi} + \frac{1}{2\pi^2}\frac{\rho Q^2}{\xi^4} + \frac{W_J}{Q}\right) + \frac{6\mu Q}{\pi \xi^2}\frac{\mathrm{d}}{\mathrm{d}s}\left(\frac{\dot{\xi}}{\xi}\right) = -\frac{\mathrm{d}}{\mathrm{d}s}\left[p_g + \frac{I\Phi}{Q} - \frac{\varepsilon_o}{2}\left(E_n^2 + (\beta - 1)E_s^2\right)\right]. \tag{3.15}$$

This equation is a transparent energy balance. On the left-hand side we find four energy sinks per unit volume, namely:

(i) surface creation against surface tension,
(ii) kinetic energy,
(iii) electric power dissipation, and
(iv) viscous dissipation.

These sinks are fed by two sources on the right-hand side:

(i) mechanical pressure,
(ii) electric power.

The total applied electric power can be calculated from the total electric charge per unit volume driven by the applied potential plus the axial component of the normal electric stress applied at the liquid surface. To simplify the expression a total applied pressure at the liquid surface is introduced,

$$p^* = p_g - \frac{\varepsilon_o}{2}\left(E_n^2 + (\beta - 1)E_s^2\right). \tag{3.16}$$

Here, the electrostatic pressure $\varepsilon_o(E_n^2 + (\beta - 1)E_s^2)/2$ has a maximum value of the order of $(\rho\sigma^2 K^2 \varepsilon_o^{-2})^{-1/3}$ (Gañán-Calvo 1997*a*, 1999, 2004), which readily gives the following weighting number to assess the relative importance of electrostatic stress over the total applied gas pressure:

$$\chi = \left(\frac{\rho\sigma^2 K^2}{\varepsilon_o^2 \Delta p_g^3}\right)^{1/3}. \tag{3.17}$$

This number is of the order unity or smaller in our experiments.

The viscous dissipation term is smaller than the kinetic energy term by a factor $1/Re$, the Reynolds number being estimated as $\rho Q H/(\mu d_j^2)$. Accordingly, dissipation becomes negligible in low-viscosity (large Reynolds number) cases. Subsequently, we will concentrate on such cases, as illustrated later (figure 12). Thus the integral contribution of viscous forces along the jet in the momentum equation (3.15) can be

neglected, so that it can be written as a Bernoulli-like integral:

$$\frac{\sigma}{\xi} + \frac{1}{2\pi^2}\frac{\rho Q^2}{\xi^4} + \frac{W_J}{Q} + p^* + \frac{I\Phi}{Q} = \text{const}, \tag{3.18}$$

where W_J is the power dissipated into heat up to the coordinate s. A careful but straightforward weighing of the terms at both ends of the domain (i.e the liquid meniscus attached to the feeding tube, and the liquid jet at the exit orifice) leads to:

$$\frac{2\sigma}{d_j} + \frac{8}{\pi^2}\frac{\rho Q^2}{d_j^4} = \Delta\Psi, \tag{3.19}$$

where $d_j = 2\xi(s = H)$ is the jet diameter at the exit orifice, and $\Delta\Psi$ is the *total available potential energy* per unit volume, expressed as:

$$\Delta\Psi = \frac{IV}{Q} - \frac{W_J(H)}{Q} + \Delta p^*. \tag{3.20}$$

Here, IV/Q, $W_J(H)/Q$ and $\Delta p^* = \Delta p_g[1 - O(\chi)]$ are the total electric power consumed, the total electrical dissipation (both per unit volume), and the total drop in the effective applied pressure at the liquid surface, between the tip of the feed tube and the exit orifice. The jet diameter d_j can thus be written, up to leading terms for the surface tension, as:

$$d_j \simeq \left(\frac{8\rho}{\pi^2\Delta\Psi}\right)^{1/4} Q^{1/2} + \frac{\sigma}{2\Delta\Psi}. \tag{3.21}$$

Following the analysis of Gañán-Calvo (1998), it is useful to define

$$d_o = \frac{\sigma}{\Delta\Psi},$$
$$Q_o = \left(\frac{\sigma^4}{\rho\Delta\Psi^3}\right)^{1/2}. \tag{3.22}$$

Using these definitions and considering the spray to be roughly monodisperse, we model the droplet diameter d_R with the Rayleigh prediction ($d_R \simeq 1.89 d_j$), d_j being the jet diameter. The resulting theoretical drop size is thus:

$$d_R \simeq 1.79\left[(Q/Q_o)^{1/2} + 0.528\right] d_o. \tag{3.23}$$

From experiments, the minimum Q/Q_o value is of the order of 7, which allows a further simplification of equation (3.23) as $d_R/d_o \simeq 1.79(Q/Q_o)^{1/2}$. Thus, from now on, the surface tension correction will be neglected. Note that our experimental choice locates EFF in a particular region of the general scaling laws for the droplet size and the emitted electric current studied by Gañán-Calvo (2004). The physical interpretation of this is the following: the jet will only issue provided capillarity is sufficiently smaller than kinetic energy, in consistency with the convective nature of jetting (e.g. Gañán-Calvo & Riesco-Chueca 2006).

3.1. *Comparison with flow focusing and electrospray results*

The jet diameter obtained with pure FF follows from (3.21) by assuming zero electric power, $\Delta\Psi = \Delta p_g$ (Gañán-Calvo 1998):

$$d_{jFF} \simeq \left(\frac{8\rho}{\pi^2\Delta p_g}\right)^{1/4} Q^{1/2}. \tag{3.24}$$

FF requires a needle-to-orifice distance H of the order of the orifice diameter D.

On the other hand, ES is characterized by a cone-to-jet transition region of characteristic length $L_t \sim Q(K\rho^2\varepsilon_o^{-1}\sigma^{-2})^{1/3}$ where the dominant transport mechanism of the current I switches from conduction in the cone to convection in the jet (Gañán-Calvo 1999). The transition region does not depend on such geometrical details as the needle diameter or its position relative to the grounded plate. A similarity structure is found at the transition region. Therefore, the physical variables, e.g. the current transported by the jet I or the jet diameter d_j, depend only on the flow rate and the liquid properties. Simulations of the transition by Hartman *et al.* (1999), Higuera (2003) and Gañán-Calvo (1999) show the electrical dissipation by the Joule effect and the electric pressure to be negligible compared with the electric power. Most of the electric power in ES is indeed carried by the tangential electric forces applied in the transition region,

$$\Delta\Psi \sim \frac{IV}{Q} \sim \left(\frac{\rho\sigma^2K^2}{\varepsilon_o^2}\right)^{1/3}, \tag{3.25}$$

where we have taken into account that the voltage drop occurs mainly in the transition region and can be estimated as $V \sim (\sigma L_t \varepsilon_o^{-1})^{1/2}$, while the current transported by the jet is $I \sim (\sigma K Q)^{1/2}$. The characteristic jet diameter in ES (see Gañán-Calvo 2004, equation (2.15)) is obtained by using (3.25) and (3.21),

$$d_{jES} \simeq \left(\frac{\rho\varepsilon_o}{\sigma K}\right)^{1/6} Q^{1/2}. \tag{3.26}$$

Figure 3 shows that, whenever H is large compared to L_t, a marked Taylor cone is formed, while the FF effect will be hard to see in the attached meniscus area. On the other hand, if $D \sim H \ll L_t$, there is not enough free distance to observe an accelerating (tapering) effect caused by the electric field, and the main tapering factor will be the co-flowing gas stream. The latter situation appears when

$$Q \gg H\left(\frac{K\rho^2}{\varepsilon_o\sigma^2}\right)^{1/3}. \tag{3.27}$$

A combined effect of gas and electric traction is only noticeable when $H \sim L_t \sim D$. If $H \leqslant L_t$, a major difference arises with the pure electrospray limit: the current transported by the jet I is not univocally determined by the transition region, but depends on the geometry and must be calculated (or measured) for the particular device and the injection conditions. However, in the pure ES limit, electric dissipation and electric pressure are assumed negligible; therefore, it seems reasonable to apply the same ideal assumptions to any intermediate (EFF) situation. Thus, defining the following dimensionless number

$$\alpha = \frac{IV}{Q\,\Delta p_g}, \tag{3.28}$$

the mass median drop size d_{REFF} expression is simplified:

$$d_{REFF} \simeq 1.8(Q/Q_o)^{1/2} d_o$$

with

$$d_o = \frac{\sigma}{\Delta p_g(1+\alpha)}, \quad Q_o = \left(\frac{\sigma^4}{\rho(1+\alpha)^3\Delta p_g^3}\right)^{1/2}. \tag{3.29}$$

The α parameter can be interpreted as a ratio of the electric energy to the mechanic energy supplied; both contributions lead to a final increase in the kinetic energy of

the jet. Very low α indicates a nearly pure FF situation, while $\alpha \gg 1$ implies we are close to a pure ES regime.

An *ad hoc* Weber number for the EFF combination, taking into account both driving terms, can be defined as

$$We_{EFF} = \frac{d_j(\Delta p_g + IVQ^{-1})}{\sigma} = 0.95(Q/Q_o)^{1/2}. \tag{3.30}$$

The EFF-Weber can be written as $We(1+\alpha)$, where We is the hydrodynamic Weber number. Axisymmetric breakup in the jetting regime involves choosing a Weber number from an intermediate range to avoid both dripping (very low Weber) and non-symmetric breakup (large Weber). Electrification contracts this range by boosting the effective Weber number (We_{EFF}). From the available literature on ES and FF, it can be gathered that ES is optimal at very low flow rates (involving a balance between electric shear and viscosity at the interface), and FF is optimal at somewhat higher flow rates (involving a Bernoulli-like effect).

Comparing expressions (3.24), (3.26) and (3.29), the following estimates are obtained for the droplet diameter ratios:

$$\frac{d_{REFF}}{d_{RES}} \sim \left(\frac{\alpha}{1+\alpha}\right)^{1/4}, \quad \frac{d_{REFF}}{d_{RFF}} \sim \frac{1}{(1+\alpha)^{1/4}}. \tag{3.31}$$

There is no single dimensionless ratio to signal the optimality of FF or ES (concerning desirable traits such as operation range, monodispersity, droplet size, ...). However, α provides a good indicator for predicting the droplet size reduction that either FF or ES alone would gain, for a given liquid and flow rate, from the combination here proposed. An FF device would experience a significant droplet size decrease upon application of a suitable voltage drop V between the liquid and the exit orifice, by choosing a large α. On the contrary, the performance of an ES device will be greatly enhanced by introducing an applied gas pressure, leading to a small α.

4. Comparison with experiments and physical discussion

We can experimentally assess the adequacy of the above approximation by careful measurement of the emitted droplet size and total electric current. In figure 9, data from figure 8 are compared, to good agreement, with the theoretical droplet size prediction (3.29). It is worth observing that this plot is scaled to encompass the whole range from pure FF to pure ES, including any intermediate EFF situation. This validates the model assumptions (i.e. neglecting viscous and electric dissipation effects, and the normal electric stress at the jet at the exit orifice).

Data dispersion is noticeably higher for Q/Q_o above about 250 (see the geometrical standard deviation GSD in figure 10). This is caused by the well-known transition from capillary axisymmetric instability to hydrodynamic instability, a transition triggered by the Weber number. Thus, for Weber numbers close to unity, an axisymmetric breakup, as predicted by Rayleigh, is to be expected. As the Weber number increases, the most probable breakup length should decrease. At a given threshold, a non-symmetric instability emerges and breakup becomes more chaotic, leading to increased droplet size dispersion. In our case, the relevant parameter is the EFF-Weber number defined in (3.30).

In FF operation, these dynamics are well established and the threshold Weber number ranges from 10 to 15 depending on the initial conditions of the jet (Gordillo *et al.* 2001). In ES applications, Rosell-Llompart (1994) showed that the threshold

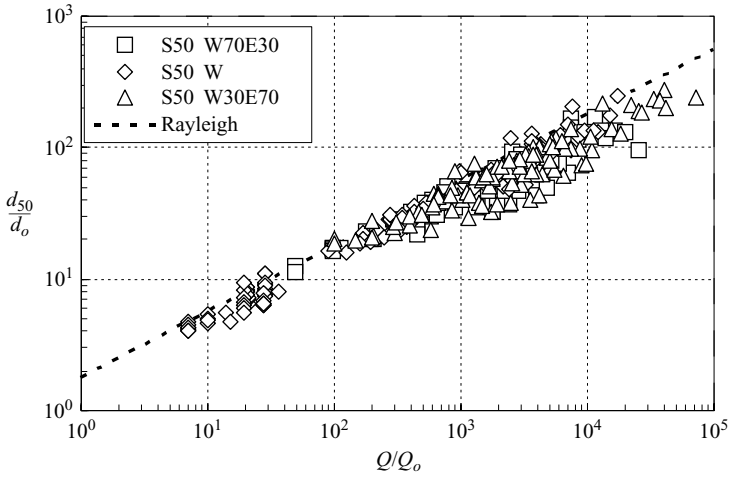

FIGURE 9. Non-dimensional droplet size *vs.* non-dimensional flow rate, using the single orifice device S50 only. Data from figure 8. The dashed line is the theoretical prediction of (3.29).

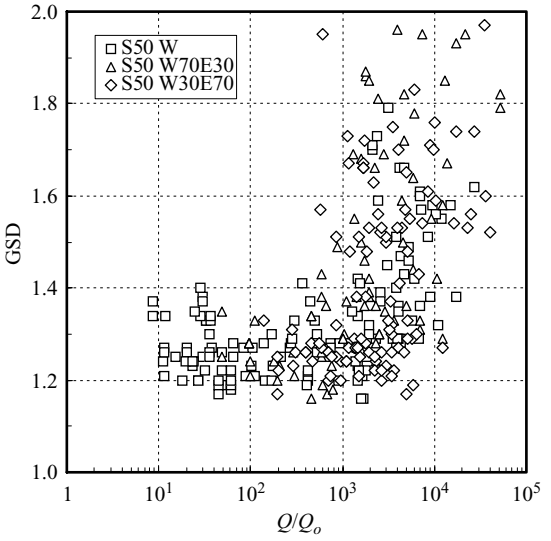

FIGURE 10. Geometrical standard deviation GSD of the droplet size as a function of the dimensionless flow rate (device S50).

Weber is surprisingly close to the FF-value (*We* about 10 to 15 as well). Consequently, in EFF operation, one should expect a deviation from the mono-disperse theoretical model at $We > 15$: this is indeed shown to be the case in figures 9 and 10 (i.e. $Q/Q_o \gtrsim 120 \rightarrow 250$). Droplet size dispersion increases sharply as *We* increases from 10 to 15, or when Q/Q_o is larger than about 250. At the other end, no measurements have been made in the dripping regime ($10 \gtrsim Q/Q_o$).

The jet current I as a function of the applied voltage V is worth studying; as pointed out above, our atomization set-up choice will be influential. Figure 11 shows the ratio of the measured EFF current to the theoretical electrospray current $I_e = 2.6(\sigma K Q)^{1/2}$. The abscissa is the ratio of the applied voltage V to the characteristic voltage drop at

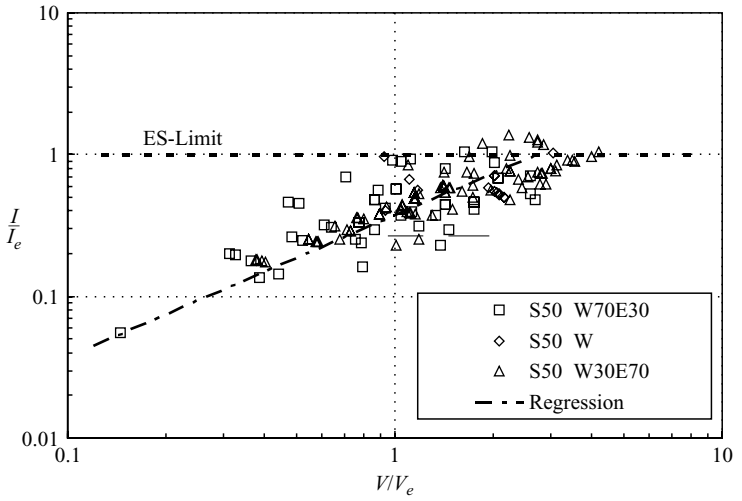

FIGURE 11. Dimensionless electric current *vs.* dimensionless potential. Dimensional data are plotted in figure 8.

the transition region in ES, V_e (see the discussion surrounding (3.25) and the estimates in Gañán-Calvo 1999):

$$V_e = \left(\frac{K\sigma\rho^2}{\varepsilon_o^4}\right)^{1/6} Q^{1/2}. \tag{4.1}$$

It can be observed that the EFF current never exceeds the ES current, $I/I_e \leqslant 1$, so that the maximum jet current is transported by pure electrospray (in the high-voltage limit, $V \gg V_e$, we can estimate $I \simeq I_e$). The most efficient electrical power transfer is achieved around ES conditions, i.e when $H \sim L$. A significant increase of V above the V_e reference is not productive in terms of EFF-performance. On the one hand, a large fraction of the electrification conveyed to the jet will be lost at the orifice plate; on the other hand, over-electrification leads to an increased EFF-Weber number, and therefore a premature onset of non-axisymmetric instability is to be expected.

Using the electrospray reference (zero pressurization) as a scaling factor is a mere convenience, as it illustrates the deviance in electric behaviour introduced by the FF effect. Note that the current converges to the ES value as the voltage is increased. A regression line is supplied as an empirical shortcut to avoid tedious current measurements in the EFF range:

$$\frac{I}{I_e} \simeq \frac{V}{2.6V_e} \rightarrow \alpha = \frac{V^2}{Q\Delta p_g}\left(\frac{K\sigma\varepsilon_o^2}{\rho}\right)^{1/3}. \tag{4.2}$$

It should, however, be kept in mind that the applicability of the regression may be restricted to the particular device (and geometry) explored by us.

4.1. *The role of the liquid viscosity*

Liquid viscosity may be influential when comparing theory and experiments. To assess the relative importance of the viscous term in the momentum equation, we recall the estimated ratio of the kinetic energy term and the viscous dissipation term leading to

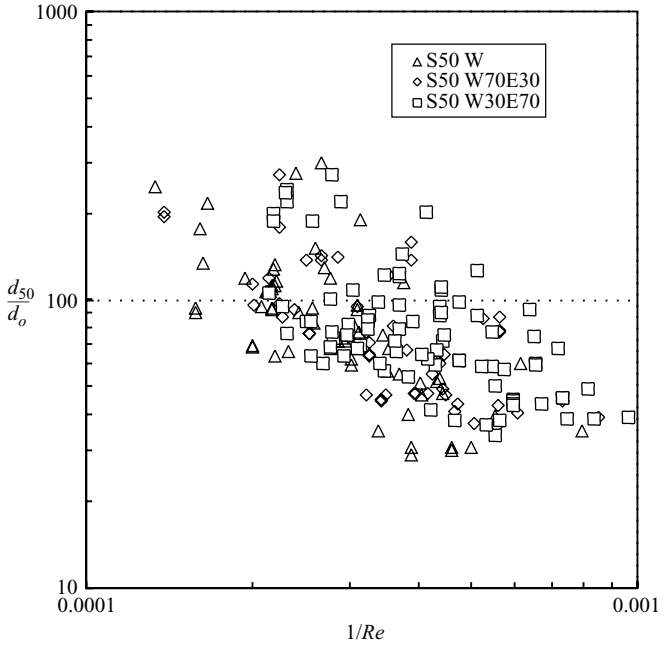

FIGURE 12. Dimensionless droplet size as a function of the Reynolds number.

(3.18). This dimensionless ratio could be written as:

$$Re \sim \frac{\rho Q H}{\mu d_j^2} \sim \frac{\rho w_j H}{\mu}. \tag{4.3}$$

where d_j and w_j are order of magnitude estimates of the jet diameter and the axial velocity at the orifice exit. This is a purely longitudinal Reynolds number, because the velocity profile is flat according to our one-dimensional assumptions.

An alternative estimate of the Reynolds number may be obtained by comparing the driving forces (gas pressure gradient and electric field) to the resisting viscosity. This parameter is defined in full analogy to the EFF-Weber number introduced in (3.30):

$$Re = \frac{\Delta p_g + IV/Q}{\mu Q/(d_j^2 H)} = \frac{[\rho \Delta p_g H^2 (1+\alpha)]^{1/2}}{\mu}. \tag{4.4}$$

Both definitions of Re are equivalent under the assumptions made in § 3.1 (negligible viscous dissipation and surface tension effects; $\chi \lesssim 1$). Indeed, the kinetic energy of the jet may be estimated as:

$$\rho w_j^2 \sim \Delta\Psi \sim \frac{IV}{Q} + \Delta p_g, \tag{4.5}$$

where the total available potential energy per unit volume $\Delta\Psi$ has been estimated with the help of (3.20). We therefore use this ratio as our EFF-Reynolds number.

The dimensionless droplet size as a function of Re for the parametrical range under study is plotted in figure 12, showing a clear downward trend of the droplet size as Re decreases. This decrease is simply due to the coupling of Reynolds and Weber numbers through the jet diameter and liquid velocity. In fact, the breakup wavelenght decreases as We increases. We fixed the tube–orifice distance H and other parameters

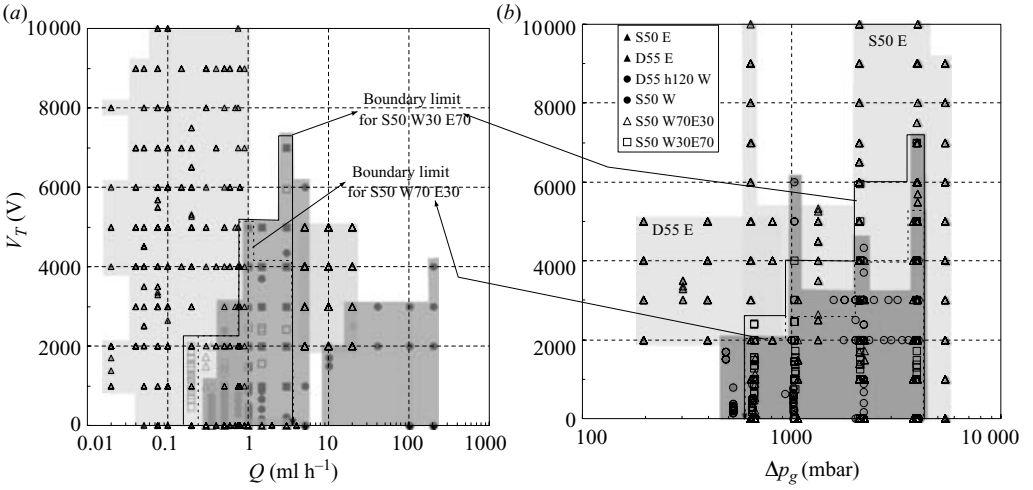

FIGURE 13. Parametrical stability regions for the liquids explored: (*a*) flow rate–voltage, (*b*) gas pressure–voltage.

while we explored various values of Δp_g, a parameter influencing both d_{50}/d_o and Reynolds.

Our experiments are limited to a narrow band in the Reynolds range, because EFF operation requires good solvents, and such liquids are, as a rule, only moderately viscous. Therefore, a weak influence on the droplet size may be anticipated. Of course, the Reynolds number could become a significant variable under different experimental conditions, e.g. were we to select a given liquid and explore a wide range of set-up parameters.

4.2. *Spraying stability*

In the parametrical study, we discarded all measurements showing any sign of spray irregularity, pulsation or dripping. We checked whether the droplet size distribution provided by Sympatec was single-peaked; in all other cases, the measurement was considered to be unstable and therefore discarded. There are many conditions for spray stability if and only if both voltage and gas pressure are jointly applied (see figure 6, where the two-peaked size distribution, at 0 V, implies instability). The spray becomes immediately unstable when switching off the voltage at fixed gas pressure, or vice versa. Figure 13 shows the approximate parametrical regions of spray stability for the liquids explored.

Therefore, the EFF combination produces droplet sizes far smaller than either flow focusing or electrospray alone could ever produce. In particular, under gas pressurization, the flow rate can be increased up to thousands of times above the maximum ES stable flow rate. Broadening the stability zone is achieved by dint of the gas stream, which skims or flushes space charge from the tip of the cone.

4.3. *The final jet surface charge. Gas ionization effects at the orifice*

This section addresses gas ionization and gas conduction effects in the region between the liquid jet and the metallic orifice plate. Silica tubing, given the voltage range in the experiments, should behave as an insulator. In addition, the orifice plate is grounded. Therefore, the only surface potentially causing gas ionization under the applied potential should be the liquid–gas interface. Using device S200G, we have carefully explored such effects at the maximum voltage ensuring stable spray emission:

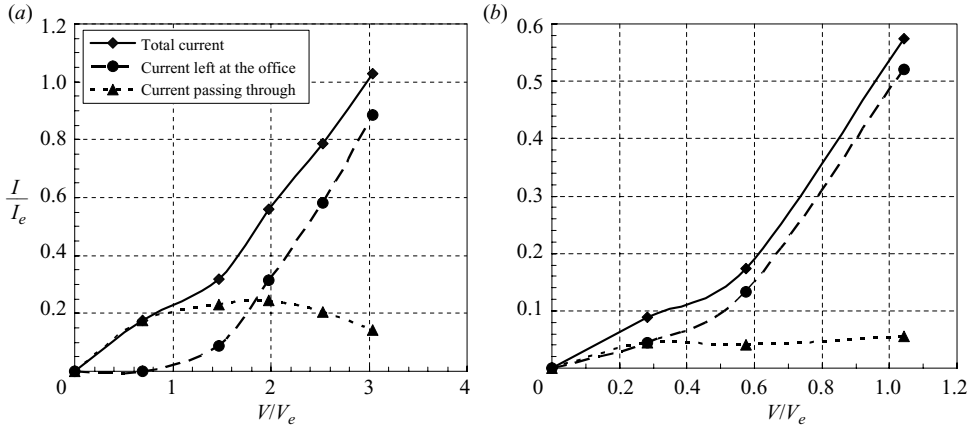

FIGURE 14. Evolution of orifice current and the impaction plate current as a function of the applied voltage, using device S50 ($H = 70\,\mu$m) and water: (*a*) $Q = 1$ml h^{-1}, $\Delta P = 3.98$ bar; (*b*) $Q = 5$ ml h^{-1}, $\Delta P = 1.28$ bar.

glimmering blue spots at the orifice edge (and, in limiting cases, at the jet surface) could be observed on a dark background. Local glow vanished when the voltage was lowered. Thereafter, using the electrical set-up of figure 5, we measured the electric current deposited at the orifice borders and at the impaction plate. The total measured electric current is the sum of both orifice and impaction plate currents. Figure 14 shows the evolution of the orifice current and the impaction plate current as a function of the applied voltage; two different conditions under positive polarity connection have been used.

Both figures show the current travelling with the jet (beyond the plate) to be substantially smaller than the current staying at the orifice plate. This is a surprising observation: conditions fostering corona effects and a simultaneous tendency to the spontaneous discharge of the liquid stream.

The most appealing interpretation of this observation is to assume that the drops are essentially discharged as they traverse the orifice plate. The discharge mechanism may be based on two effects *a*) strong field induction between the jet and the plate; *b*) ionic evaporation of the drops under the intense electric field at the orifice, leading to gas ionization. The first explanation may be more appropriate for the main liquid stream and the principal drops; while evaporation is likely for satellite drops. As explained in López-Herrera & Gañán-Calvo (2004), most of the electric transport in ES is carried by the principal drops, but even a weak amount of ionic evaporation may lead to the gas becoming a good conductor by chain reaction ionization. Thus, an intense collaborative effect between those two possible causes may take place, leading to discharge. The reproducibility of the discharge effect has been checked under a wide range of situations. It is worth emphasizing that EFF discharge takes place without the need for any external means, countrarily to that required in pure electrospraying operation.

The induction/evaporation theory is strengthened by the fact that no liquid drops above 0.5 μm are observed to hit the orifice borders (in addition, drops smaller than the main ones were shown by López-Herrera & Gañán-Calvo (2004) to carry only a negligible fraction of the total current). We were able to exclude such occurrence altogether by using the glass window of device S200G (see figures 4 and 3). In the event

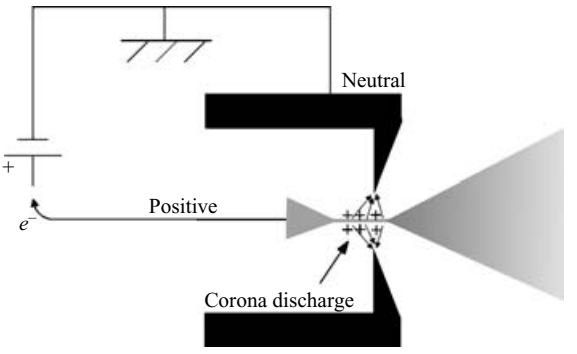

FIGURE 15. Corona discharge phenomenon under positive polarity.

of liquid impaction, some remnants in the orifice borders and liquid spitting from the orifice exit ought to be observed. All the data presented in this study, including those of figure 14, have been collected under operational conditions excluding such occurrences. When the applied voltage reached a limiting value, we always observed that the jet began to deviate from the symmetry axis and the issuing spray showed pulsation and spitting. A similar phenomenon is reported in classical electrospray, i.e. the jet deviates from the axis of symmetry when the voltage is raised above a certain limit (Cloupeau & Prunet-Foch 1989, 1994). At this point, we discarded the corresponding measurement and a different flow/pressure or smaller voltage condition was set.

A further consideration may be included with respect to jet discharge by the plate orifice. Gas conduction effects should take place at jet regions close to the exit orifice. This is consistent with, given our experimental set-up, the minimum distance from any point of the liquid surface to the orifice border occuring at the jet surface close to the exit orifice section; the probability of gas discharge is at a maximum there. We therefore assume the appearance of a strong electric field induced by the passing jet or charged droplet stream at the plate orifice borders, together with local gas ionization effects, to be the main causes for droplet discharge (see figures 14 and 15) under positive polarity connection.

In general, residual droplet charge becomes smaller as the gas pressure decreases and the liquid flow rate increases. This is consistent with two simple and solid facts: (i) the larger the gas pressure, the weaker the corona discharge effects (under a high gas pressure, more intense electric fields are required for gas corona discharge), and (ii) the larger the liquid flow rate, the larger the jet radius and the closer the jet to the orifice edge.

Therefore, EFF contributes two key features: a pressurization effect from the focusing gas; and a screening effect from the orifice plate. Both traits tend to limit the output electric current transported by the issuing droplets.

These observations are restricted to positive polarity connection. The effect of a negative polarity connection is left for further work. We may advance that we have observed a negative polarity voltage range for which completely neutralized droplets issue from the orifice.

4.4. *Multiple orifice EFF*

The effects of a multi-orifice configuration can be explored by studying droplet size in a device with 55 orifices and $D = 200\,\mu\text{m}$, arranged in a hexagonal array with a cell-to-cell distance of 1.8 mm. Figure 16 shows the spray plume in two different voltage conditions.

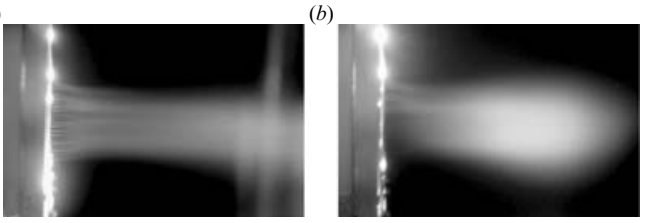

FIGURE 16. Ethanol spray as issued from device D55 for $Q = 50\,\mathrm{ml\,h^{-1}}$, $\Delta P = 530\,\mathrm{mbar}$, with: (*a*) 0 V, (*b*) 1130 V.

As a preliminary oddity, in the case of a neutral connection (0 V), we observe the spray column becoming narrower at distances from the exit orifice section of the order of the total array diameter and above. Such behaviour is observed in all experimental conditions where a neutral spray issues from this kind of device (several have been built and tested). A plurality of liquid sources gives rise to a competition among the jets for momentum and energy exchange with a shrinking ambient. A tapering spray column obviously increases the chance of droplet coalescence, but also favours droplet breakup owing to the greatly delayed turbulent decay of the compound gas jet: as a result, a droplet size probability distribution function with a wider dispersion and a smaller average is observed.

However, see figure 16*b*, when an electric voltage is applied, the spray column is expansive, so that droplet coalescence becomes more unlikely, owing to residual droplet charge (Coulombic repulsion). Droplet size decreases (compared with a single orifice device) as a consequence of the enhanced turbulence of the compound gas jet, with a smaller chance of droplet coalescence compared to unelectrified devices. As a result, a remarkably fine spray with a significant yield is obtained with this device.

5. Conclusions

We have presented a new liquid ultra-fine atomization method and device combining the advantages of electrospray and flow focusing. For the same liquid flow rate, significantly smaller droplet sizes are obtained as in pure ES or FF applications. For any given liquid, EFF is able to handle liquid flow rates (or total yield) much larger than allowable under the stability requirements of electrospray. In EFF, the hydrodynamic pattern borrowed from FF is instrumental as a means to flush space charges and to screen the downstream jet from the upstream electrified area around the meniscus. As an extraordinary spinoff effect we report that, when the device is operated under the appropriate applied voltage range, it also yields an almost unelectrified spray without the need for any external discharging means.

We provide about two thousand droplet size measurements using different liquids. The droplet charge is also studied in a more detailed analysis. In addition, a theoretical model is developed leading to a comprehensive Euler–Bernoulli-like energy balance along the streamline: it can be used to predict the droplet size (equation (3.29)) to good agreement with the experimental measurements for an ample range of device geometries. The total electric current transport can also be correlated with the theoretical electrospray current $I_e = 2.6(\sigma K Q)^{1/2}$.

A combined Weber number can be introduced, signalling the risk of dripping (at the lower end) or asymmetric breakup (at $Q/Q_o \gtrsim 250$). In addition, a dimensionless parameter α (the ratio of the electric energy to the mechanic energy supplied) provides

a suitable indicator covering the whole range from pure FF to pure ES, crossing over intermediate EFF situations.

Finally, we emphasize the following features of this controllable, simple and reproducible EFF technique:

(i) Fine droplet size, in the micron and sub-micron range: significantly smaller droplet sizes as in pure FF.

(ii) Enhanced robustness and stability (with respect to pure ES): (*a*) start-up and stop regimes are reduced to a minimum thanks to the flushing effect of the gas, (*b*) the liquid flow rates can be many orders of magnitude larger than in pure ES (forced gas flow flushes space charge issued from liquid–gas interfaces).

(iii) Wider operation range as in FF or ES.

(iv) The orifice plate provides an implicit, extremely simple way to discharge the droplets without the need for external means such as radioactive sources or discharging needles.

(v) The EFF-set-up is readily amenable to multiplexing.

The authors are grateful for the support of the Ministry of Science and Technology of Spain, grant DPI2002-04305-C02-02. Valuable experimental assistance was provided by Mr Javier Zamora Martín, to whom we are indebted.

REFERENCES

Bailey, A. G. 1988 *Electrostatic Spraying of Liquids*. John Wiley.

Basaran, O. A. 2002 Small-scale free surface flows with breakup: Drop formation and emerging applications. *AIChE J.* **48**, 1842–1848.

Berkland, C., Pack, D. W. & Kim, K. 2004 Controlling surface nano-structure using flow-limited field-injection electrostatic spraying (FFESS) of poly(D,L-lactide-co-glycolide). *Biomaterials* **25**, 5649–5658.

Chen, D. R., Pui, D. Y. H. & Kaufman, S. L. 1995 Electrospraying of conducting liquids for monodisperse aerosol generation in the 4 nm to 1.8 μm diameter range. *J. Aerosol Sci.* **26**, 963–977.

Cherney, L. T. 1999*a* Electrohydrodynamics of electrified liquid menisci and emitted jets. *J. Fluid Mech.* **378**, 167–196.

Cherney, L. T. 1999*b* Electrohydrodynamics of electrified liquid menisci and emitted jets. *J. Aerosol Sci.* **30**, 851–862.

Cloupeau, M. & Prunet-Foch, B. 1989 Electrostatic spraying of liquids in cone-jet mode. *J. Electrostatics* **22**, 135–159.

Cloupeau, M. & Prunet-Foch, B. 1994 Electrohydrodynamic spraying functioning modes: a critical review. *J. Aerosol Sci.* **25**, 1021–1036.

Cohen, I., Li, H., Hougland, J. L., Mrksich, M. & Nagel, S. 2001 Using selective withdrawal to coat microparticles. *Science* **292**, 265–267.

Eggers, J. 1997 Nonlinear dynamics and breakup of free-surface flows. *Rev. Mod. Phys.* **69**, 865–929.

Eggers, J. & Dupont, T. F. 1994 Drop formation in a one-dimensional approximation of the Navier–Stokes equations. *J. Fluid Mech.* **262**, 205–221.

Feng, J. J. 2002 The stretching of an electrified non-Newtonian jet: a model for electrospinning. *Phys. Fluids* **14**, 3912–3926.

Fenn, J. B., Mann, M., Meng, C. K., Wong, S. F. & Whitehouse, C. M. 1989 Electrospray ionization for mass-spectrometry of large biomolecules. *Science* **246**, 64–71.

Fernández de la Mora, J. & Loscertales, I. 1994 The current emitted by highly conducting Taylor cones. *J. Fluid Mech.* **260**, 155–184.

Gamero-Castaño, M. & Hruby, V. 2002 Electric measurements of charged sprays emitted by cone-jets. *J. Fluid Mech.* **459**, 245–276.

Gañán-Calvo, A. M. 1997*a* Cone-jet analytical extension of Taylor's electrostatic solution and the asymptotic universal scaling laws in electrospraying. *Phys. Rev. Lett.* **79**, 217–220.

Gañán-Calvo, A. M. 1997*b* On the theory of electrohydrodynamically driven capillary jets. *J. Fluid Mech.* **335**, 165–188.

Gañán-Calvo, A. M. 1998 Generation of steady liquid microthreads and micron-sized monodisperse sprays in gas streams. *Phys. Rev. Lett.* **80**, 285–288.

Gañán-Calvo, A. M. 1999 The surface charge in electrospraying: its nature and its universal scaling law. *J. Aerosol Sci.* **30**, 863–872.

Gañán-Calvo, A. M. 2004 On the general scaling theory for electrospraying. *J. Fluid Mech.* **507**, 203–212.

Gañán-Calvo, A. M. & Barrero, A. 1999 A novel pneumatic technique to generate steady capillary microjets. *J. Aerosol Sci.* **30**, 117–125.

Gañán-Calvo, A. M. & Riesco-Chueca, P. 2006 Jetting–dripping transition of a liquid jet in a lower viscosity co-flowing immiscible liquid: the minimum flow rate in flow focusing. *J. Fluid Mech.* **553**, 75–84.

Gañán-Calvo, A. M., Lasheras, J. C., Dávila, J. & Barrero, A. 1994 The electrostatic spray emitted from an electrified conical meniscus. *J. Aerosol Sci.* **24**, 1121–1142.

Gañán-Calvo, A. M., Dávila, J. & Barrero, A. 1997 Current and droplets size in the electrospraying of liquid. Scaling laws. *J. Aerosol Sci.* **28**, 249–275.

García, F. J. & Castellanos, A. 1994 One-dimensional models for slender axisymmetrical viscous-liquid jets. *Phys. Fluids* **6**, 2676–2689.

Gautam, A., Waldrep, J. C. & Densmore, C. L. 2003 Aerosol gene therapy. *Mol. Biotechnol.* **23**, 51–60.

Gordillo, J. M., Pérez-Saborid, M. & Gañán-Calvo, A. M. 2001 Linear stability of co-flowing liquid–gas jets. *J. Fluid Mech.* **448**, 23–51.

Hartman, R. P. A., Brunner, D. J., Camelot, D. M. A., Marijnissen, J. C. M. & Scarlett, B. 1999 Electrohydrodynamic atomization in the cone–jet mode physical modeling of the liquid cone and jet. *J. Aerosol Sci.* **30**, 823–849.

Higuera, F. 2003 Flow rate and electric current emitted by a Taylor cone. *J. Fluid Mech.* **484**, 303–327.

Hohman, M. M., Shin, M., Rutledge, G. & Brenner, M. P. 2001 Electrospinning and electrically forced jets. ii. Applications. *Phys. Fluids* **13**, 2221–2236.

Howard, K. A. & Alpar, H. O. 2002 The development of polyplex-based DNA vaccines. *J. Drug Targeting* **55**, 237–245.

Jayan, N. & Raghunandan, B. N. 2003 A technique for drop size control during throttling of a rocket engine. *Atom. Sprays* **13**, 345–355.

Landau, L. D. & Lifshitz, E. M. 1960 *Electrodynamics of Continuous Media.* Pergamon.

Laryea, G. N. & No, S. Y. 2003 Development of electrostatic pressure-swirl nozzle for agricultural applications. *J. Electrostat.* **57**, 129–142.

Lasheras, J. C., Villermaux, E. & Hopfinger, E. J. 1998 Break-up and atomization of a round water jet by a high-speed annular air jet. *J. Fluid Mech.* **357**, 351–379.

Lawley, A. & Leatham, A. G. 1999 Spray forming commercial products: principles and practice. *Adv. Powder Technol.* **299**, 407–415.

Lee, H. C. 1974 Drop formation in liquid jets. *IBM J. Res. Develop.* **18**, 364–369.

Lefevbre, A. H. 1989 *Atomization and Sprays.* Hemisphere.

López-Herrera, J. M. & Gañán-Calvo, A. M. 2004 A note on charged capillary jet breakup of conducting liquids. Experimental validation of a viscous one dimensional model. *J. Fluid Mech.* **501**, 303–326.

López-Herrera, J. M., Gañán-Calvo, A. M. & Perez-Saborid, M. 1999 One-dimensional simulation of the breakup of capillary jets of conducting liquids. Application to E H D spraying. *J. Aerosol Sci.* **30**, 895–912.

López-Herrera, J. M., Riesco-Chueca, P. & Gañán-Calvo, A. M. 2005 Linear stability analysis of axisymmetric perturbations in imperfectly conducting liquid jets. *Phys. Fluids* **17**, 034106.

Melcher, J. R. 1981 *Continuum Electromechanics.* M I T Press, Cambridge, Massachusetts.

Melcher, J. R. & Warren, E. P. 1971 Electrohydrodynamics current carrying semi-insulating jet. *J. Fluid Mech.* **47**, 127–143.

Notz, P. K. & Basaran, O. A. 1999 Dynamics of drop formation in a electric field. *J. Colloid Interface Sci.* **213**, 218–237.

Pantano, C., Gañán-Calvo, A. M. & Barrero, A. 1994 Zeroth order, electrohydrostatic solution for electrospraying in cone–jet mode. *J. Aerosol Sci.* **25**, 1065–1077.

Rosell-Llompart, J. 1994 Size characterization in electrosprays of submicron droplets. PhD thesis, Yale University.

Rosell-Llompart, J. & Fernández de la Mora, J. 1994 Generation of monodisperse droplets 0.3 to 4 μm in diameter from electrified cone-jets of highly conducting and viscous liquids. *J. Aerosol Sci.* **25**, 1093–1119.

Saville, D. A. 1997 Electrohydrodynamics: the Taylor–Melcher leaky dielectric model. *Annu. Rev. Fluid Mech.* **29**, 27–64.

Schulkes, R. M. S. M. 1994 The evolution and bifurcation of a pendant drop. *J. Fluid Mech.* **278**, 83–100.

Taylor, G. I. 1964 Disintegration of water drops in a electric field. *Proc. R. Soc. Lond.* A **280**, 383–397.

Wilkes, E. D., Phillips, S. D. & Basaran, O. A. 1999 Computational and experimental analysis of dynamics of drop formation. *Phys. Fluids* **11**, 3577–3598.

Yildirim, O. E. & Basaran, O. A. 2001 Deformation and breakup of stretching bridges of Newtonian and shear-thinning liquids: comparison of one- and two-dimensional models. *Chem. Engng Sci.* **56**, 211–233.

Zhang, D. F. & Stone, H. A. 1997 Drop formation in viscous flows at a vertical capillary tube. *Phys. Fluids* **9**, 2234–2242.